Journal of Non-Crystalline Solids xxx (xxxx) xxx-xxx

Contents lists available at ScienceDirect

Journal of Non-Crystalline Solids

journal homepage: http://ees.elsevier.com

Mechanical and transport properties of fibrous amorphous silica meshes and membranes fabricated from compressed electrospun precursor fibers

Andrei Stanishevsky*, Justin Tchernov

Department of Physics, University of Alabama at Birmingham, 1300 University Boulevard, Birmingham, AL 35294, USA

ARTICLE INFO

Keywords
Amorphous silica
Nanofibers
Electrospinning
Tensile properties
Flow permeability

ABSTRACT

Highly porous, 0.1–1.5 mm thick fibrous amorphous silica (FAS) meshes with 500 ± 200 nm fiber diameters were prepared from the precursor fibers made by a high-yield free-surface alternating field electrospinning (AFES) process. A combination of mild thermal and pressure treatment of the fibrous precursor material before the calcination step was used to tailor the mechanical and transport properties of the resulting FAS structures. Compression of the as-spun material determined the resulting porosity, effective fiber diameter, and microarchitecture of the FAS structures when calcined between 600 and 1000 °C. Flexible FAS meshes and membranes revealed the tensile strength and modulus up to 1.4 MPa and 580 MPa, respectively, and Darcy'S permeability coefficient in a range of 1.2×10^{-12}–1.6×10^{-11} m^2. Taking into consideration the compression-dependent effective fiber diameter, the permeability of compressed FAS membranes fitted the models developed for two-dimensional fibrous layer architectures with partial fiber alignment within the stacked layers.

1. Introduction

Fibrous materials prepared by electrospinning have been demonstrated as promising membrane materials for many demanding applications in filtration, separation, adsorption, catalytic, and other processes [1–7]. Electrospun fibrous materials with fiber diameters ranging from tens of nanometers to a few micrometers exhibit typically high porosities (more than 80%) with relatively uniform sizes and high interconnectivity of pores. These materials can also be post-treated to modify their textural and mechanical properties or to induce specific surface functionality for improved efficiency and performance [6,7].

Almost all polymeric, inorganic and composite electrospun fibrous materials are prepared from polymeric liquid precursors [6–8]. While the electrospun polymeric fibrous materials can be used directly as membrane structures, the fabrication of inorganic membranes requires thermal processing to remove the organic component. Thermal processing adds more challenge to the development of fibrous inorganic materials with controllable structure, mechanical integrity, and desired functionalities.

In recent years, many nano- and micro-fibrous inorganic membrane structures have been fabricated for different purposes from electrospun precursors, including ceramic [9–15], composite [16,17] and amorphous silica-based [10,18–26] fibrous materials. For example, nanofibrous ZrO_2 [11] and Zr:TiO_2 [12] ceramic membranes for efficient air filtration and water purification, respectively, have been demonstrated. Tang et al. [13] prepared high-flux fibrous ZrO_2 membranes with pore sizes in a range of 0.2–1.6 μm and a high specific surface area for adsorption and separation processes. Santos et al. [14] demonstrated the efficiency of nanofibrous Ti_4O_7 membranes for water purification using phenol as a model contaminant. Fu et al. [15] achieved 97.7% of oil/water separation efficiency and 98% of organic dye capture with fibrous TiO_2/Al_2O_3 fibrous membranes. In another study, high oil/water separation efficiency has been also shown with free-standing flexible fibrous glassy carbon-silica composite membranes [16]. High-strength flexible nanofibrous SiOC membrane structures have been demonstrated by Wu et al. [17].

Amorphous silica and silica-based fibrous materials account for a large fraction of research on inorganic membranes made from electrospun precursors. For example, Wang et al. [18] developed fibrous MnO_2/SiO_2 catalytic membranes for wastewater remediation, while Si et al. [19] prepared multifunctional flexible and magnetic nanofibrous $NiFe_2O_4/SiO_2$ membranes with good mechanical strength. Very flexible and porous zirconia-doped silica 1 mm-thick nanofibrous membranes with 0.25 MPa tensile strength were fabricated by Tang [20]. Membranes made of pure fibrous amorphous silica have also been a subject of a number of studies [21–25]. Nanofibrous amorphous silica usually displays strong chemical resistance, high thermal stability, flexibility, and good mechanical strength that can reach up to 5.5 MPa in tension [21–23]. Such glassy material has shown, for example, strong potential

---

* Corresponding author at: Department of Physics, University of Alabama at Birmingham, 1300 University Boulevard, CH 342, Birmingham, AL 35294-1170, USA.
E-mail address: astan@uab.edu (A. Stanishevsky)

https://doi.org/10.1016/j.jnoncrysol.2019.119653
Received 18 May 2019; Received in revised form 23 August 2019; Accepted 26 August 2019
Available online xxx

as high-flux oil-water [24,25], toluene-water and ethanol-hexane [26] separation membranes.

The fabrication of inorganic fibrous membranes, in particular silica-based, from electrospun precursors faces many challenges associated with the preparation and calcination of precursor materials, control of mechanical and transport properties, structure modification and functionality, as well as with fabrication productivity and cost. Both the evaporation of solvent during the precursor fiber formation and decomposition of the precursor components during calcination affect the microstructure of the final inorganic fibers and can lead to porous fibers and microcracks resulting in a brittle fibrous assembly with low strength. Most precursor materials to prepare fibrous amorphous silica have been made by using a capillary needle direct-current (DC) electrospinning. The process provides good control of the precursor fiber composition, diameter, textural properties, and assemblage but it is very slow [6–8]. The assembly of precursor fibers into a fibrous construct becomes very different when the process scales up. The precursor fiber packing and interaction in as-spun fibrous constructs can strongly impact calcination and the resulting microarchitecture of the final inorganic membrane structure. In addition, some inorganic nanofibrous meshes have been shown to be flexible and soft. This makes the inorganic nanofibrous materials easily compressible, and it can decrease their performance under increased pressure [27]. Understanding the impact of this factor is also important for the process upscaling and development of commercial nanofibrous membrane structures.

The current study presents the first results on the mechanical properties and air permeability of highly porous fibrous amorphous silica (FAS) meshes and membranes fabricated from precursor fibrous material prepared by a high-yield free-surface alternating field electrospinning (AFES) process. This electrospinning technique generates dense fibrous flows where the propagating fibers carry almost no electric charge [28]. Combined with a high rate of fiber production, the process also provides more flexibility in the collection and handling of fibers. AFES has been demonstrated for the fabrication of several types of polymers [29,30] and ceramic [31,32] nanofibers. It has been shown that both nanofibrous polymeric and ceramic mesh structures with good mechanical integrity can be made from AFES precursor fibers. AFES silica precursor fibers in this work were additionally post-processed using an uncommon warm-pressing procedure to create, after a calcination step, FAS meshes with different porosities. The fabrication process and the effect of the precursor material compression on the porosity, compressibility, tensile strength and modulus, and air permeability of FAS membrane structures are analyzed and discussed in sections below.

2. Experimental

2.1. Preparation of fibrous amorphous silica (FAS) meshes

The precursor for nanofibrous silica was based on tetraethoxysilane (TEOS, $Si(OC_2H_5)_4$, 99%+, Alfa Aesar) and Polyvinyl butyral (PVB, M_w ~70,000, 80% butyral, Scientific Polymer Products, Inc). Hydrochloric acid (5 N) and ethanol (200 proof) were supplied by Fischer Scientific and Decon Labs, Inc., respectively. DI water was produced on site. TEOS was dissolved in ethanol and then DI water/HCl mixture was added under magnetic stirring to prepare a sol with the TEOS/ethanol/H_2O/HCl molar ratio of 1.0/2.0/2.0/0.01 according to the procedure described in [33]. Then, 15 wt% PVB solution in ethanol was added to the obtained silica sol to achieve the polymer concentration of 4.75 ± 0.5 wt%. The precursor sol (silica yield ~100 mg/mL) was stored at normal laboratory conditions and it was stable for at least three months.

The precursor solution was delivered to the fiber-generating electrode of a free surface alternating field electrospinning (AFES) apparatus [30,31]. A precursor fiber productivity of ~12 g/h was achieved with a 25-mm diameter and 1.5-mm deep dish-like electrode head, a precursor delivery rate of ~60 mL/min, and 25 kV rms voltage. The generated precursor fibers were collected on a rotating 10-cm diameter plastic drum until a 1.0–2.0 mm thick fibrous layer (or mesh) was spun. The collected meshes were stabilized at 60 °C overnight and then cut into $3.0 \times 14.0\,\mathrm{cm}^2$ sheets. Those meshes were placed on a hot plate and warm-pressed at 200 °C for 4 h. Ceramic blocks were used as the load, and Teflon spacers with different thicknesses between 0.1 and 1.5 mm controlled the limit of compression. After the compression step, the load was removed and the fibrous meshes were moved to a programmable furnace (Isotemp, Fisher Scientific), where they were heated at 5 °C/min and calcined at 600, 800, and 1000 °C for 2 h. The resulting FAS meshes with thicknesses in a range of 0.17–1.5 mm were cut into small strips and circular FAS membranes for tensile and permeability tests, respectively. The dimensions and mass were measured for each FAS specimen to obtain accurate data for the characterization.

2.2. Characterization techniques

Fourier Transform Infrared (FTIR) spectra of calcined amorphous silica fibers were recorded with Vertex 70 FTIR spectrometer (Bruker Optics) in transmission mode using an average of 32 scans and a resolution of $4\,\mathrm{cm}^{-1}$ for each sample.

X-ray diffraction (XRD) patterns of nanofibrous amorphous silica were obtained using a PANalytical X'Pert Pro MPD diffractometer (Cu Kα tube operated at 40 kV and 45 mA, the Bragg–Brentano geometry, PANalytical X'Celerator detector). Data were acquired over the range of 5–90° 2θ using the step of 0.0167° and dwelling time of 27 s. Crushed samples were pressed into zero-background silicon holders and rotated during the measurements to minimize the possibility of preferred orientation effects. The Scherrer equation [34] was used to calculate the size of ordered silica domains.

The fiber diameter, surface morphology, and arrangement in calcined FAS meshes were investigated by scanning electron microscopy (field-emission scanning electron microscope FEI Quanta 650 FE-SEM). SEM imaging was done in secondary electron mode, at an accelerating voltage of 15 kV, electron probe current 2 μA, and a chamber pressure of 1×10^{-4} Pa. SEM samples were made by cleaving the FAS meshes frozen with liquid nitrogen. The samples were sputter coated with ~5 nm AuPd layer to reduce electric charging. SEM images were analyzed using ImageJ image processing program to determine the fiber diameter. At least 50 fibers in 2–3 images were analyzed for each sample.

Tensile moduli and strength of FAS meshes were determined using a custom made microtensile tester based on DFG35-10 force gauge (1.0 mN resolution, 1 N load cell, Omega Engineering, Inc.) and motorized ThorLab MT1-Z8 precision stage (100 nm minimum step). The data were corrected for the load cell deflection and initial position of the stage. At least 5 specimens were cut from random locations along and across each FAS mesh (~$2.5 \times 11\,\mathrm{cm}^2$ size) with different thicknesses and calcination temperatures. The same measurements were also performed using ADMET eXpert 4000 microtester (ADMET, Inc.) equipped with 5 N load cell and MTESTQuattro controller. In both cases the specimens with the 4–6 mm width and gauge length of 10–20 mm were tested at 0.05 mm/s loading rate. The data were corrected for the load cell deflection and initial position of the stage. The dimensions and mass of each sample were determined individually using a digital micrometer, caliper and precision balance.

Porosity of FAS meshes was evaluated according to the formula.

$$\varepsilon = \left(1 - \rho_{\mathrm{exp}}/\rho_{\mathrm{silica}}\right) \times 100\% \tag{1}$$

where ρ_{exp} is the apparent density of the fibrous material and ρ_{sil}-

$_{\mathrm{ica}} = 2.196\,\mathrm{g/cm^3}$ is the density of non-porous amorphous silica. To determine the mass density, the thickness of the samples was measured by a calibrated clamping micrometer with the spring removed to reduce the sample deformation and by an optical microscope with a calibration grid. The thickness data were based on five tests at different locations of each of five ~25 × 25 mm^2 samples cut of a larger mesh. Lateral dimensions of the samples were assessed using a caliper, and the mass was determined by a digital Sartorius Entris 90 mm precision balance with 0.1 mg resolution.

Air flow permeability of nanofibrous amorphous silica membranes was determined according to Darcy's law [35]:

$$k_D = \mu h Q / (A \Delta P) \tag{2}$$

where h is the membrane (mesh) thickness in meters, Q is the air flow rate in m^3/s, A is the area in m^2, μ is the viscosity (1.847×10^{-5} Pa·s for air at 25 °C), and ΔP is the pressure drop across the membrane. A custom, 10-mm diameter open area, membrane capillary flow test cell similar to those described in [36,37] was used for these tests.

3. Results and discussion

The preparation of fibrous assemblies in AFES process differs from traditional constant voltage DC-electrospinning. The propagation of generated precursor fibers in AFES relies on a strong ionic wind phenomenon [38]. It results in a dense, frequently tubular and slowly moving (0.2–1.2 m/s) flow of precursor fibers that carry almost no electric charge. Such fibrous flow can be easily captured on any substrate, like in the case of silica/PVB precursor fibers accumulated on a plastic drum (Fig. 1a). The resulting fibrous precursor meshes can be annealed in a range from 600 °C to 1000 °C with little change in the material appearance (Fig. 1b). Calcination step reduces the mass of initial fibrous mesh approximately two times. The calcined FAS meshes shrunk both 20 ± 3% along each side and 10 ± 2% in thickness and remained flexible. The areal density of calcined FAS meshes was in the range 25–30 g/m^2, depending on the variations in the speed of both the flow and collector.

It has been noticed that by applying ~10 kPa pressure to as-spun fibrous precursor meshes they can be compressed to ~12% of their initial thickness. When pressure is removed, the material recovers to ~65% of its initial thickness. It required at least twice as much pressure to obtain the same compression of the 600 °C calcined FAS meshes. However, calcined fibrous meshes recover to 85% of their initial thickness. When the fibrous precursor material was warm-pressed, the compressed meshes showed much smaller thickness recovery when the load was removed. This allowed a series of FAS meshes with mass densities between 0.015 ± 0.004 and 0.22 ± 0.002 g/cm^3 (corresponding porosity is ~99.3–90%) to be prepared for each calcination temperature (Fig. 1c). Because the thickness of denser amorphous silica meshes can be measured quite accurately, the density *vs* thickness graphs provided verification of the thicknesses for the least dense meshes.

XRD patterns of calcined fibrous material revealed a broad characteristic peak that indicates an amorphous silica structure with the presence of a short-range order in atomic clusters (Fig. 2a). The 2θ peak position changes from 21.7° to 21.1° and the apparent cluster size slightly increases, respectively, from 0.9 nm for 600 °C to 1.2 nm for 1000 °C calcined silica. Such trends have been associated with the structural rearrangement in a cristobalite-like structure of a SiO$_2$ cluster network [39]. FTIR spectra (Fig. 2b) indicate the presence of silanol groups (Si-OH) in the FAS calcined at 600 °C. Otherwise, there is little difference in the absorption peak position and intensity for FAS cal-

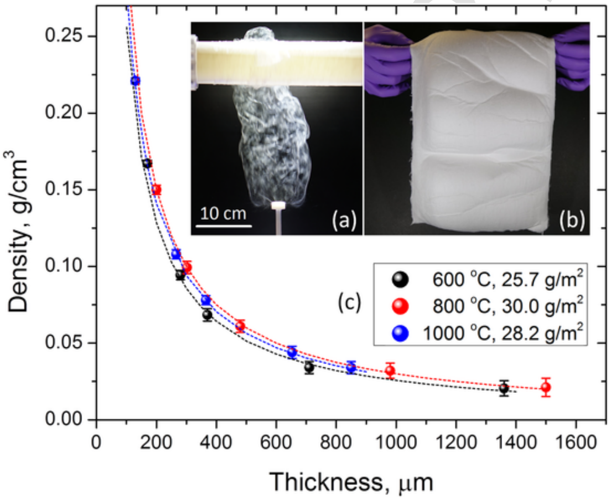

Fig. 1. (a) AFES generated flow of precursor fibers is collected on a plastic drum; (b) Non-compressed 1.5 mm thick FAS mesh calcined at 600 °C; (c) Mass density of the calcined FAS meshes *vs* thickness of the compressed material (Note the difference in the initial thickness and areal density of the FAS meshes).

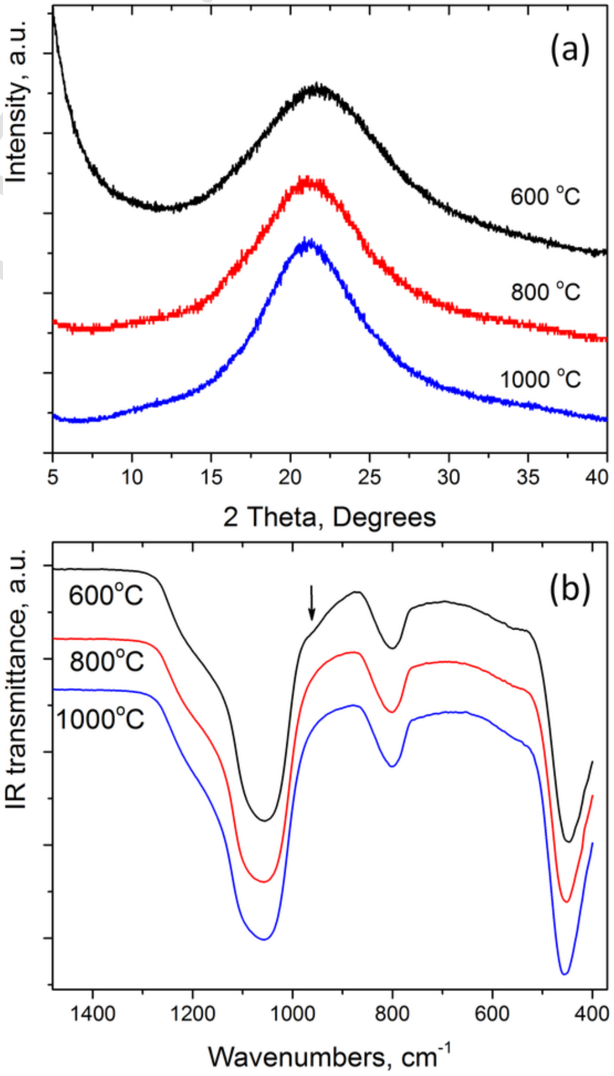

Fig. 2. (a) XRD patterns and (b) FTIR spectra of fibrous amorphous silica after calcination at 600, 800, and 1000 °C. The arrow indicates infrared absorption due to Si–OH group.

cined at all used temperatures. This further confirms the structural similarity of fibrous amorphous silica calcined between 600 and 1000 °C.

SEM analysis of the both non-compressed and compressed FAS meshes (Fig. 3) showed a predominantly random in-plane arrangement of fibers (Fig. 3c,f). The fibers are aligned almost parallel to the plane of mesh across the thickness of material (Fig. 3b,e), regardless of whether the material was compressed or not. It was still possible to split the meshes into 10–50 μm thick flakes, which indicates relatively weak out-of-plane bonding between the fibers, especially in non-compressed material. Hence, such microarchitecture can be described as a layered two-dimensional random fibrous network. Fiber diameters of 500 ± 200 nm were measured from the SEM images of 600 °C calcined non-compressed FAS material. There was only slight reduction of the fiber diameters observed after the calcination at 800 and 1000 °C. However, the fiber diameters were seemingly larger (700–1200 nm) inside the fibrous layer (Fig. 3b) and when the material was compressed (Fig. 3e,f). This is associated with the fact that the precursor fibers become more bundled and partially fused inside the fibrous layer during collection and warm-pressing. Partial bundling of precursor fibers can also occur in the dense fibrous flow generated by AFES [29–32]. The presence of residual solvent in the fibrous layer collected at a high rate induces some additional bundling and fusion of fibers. The softening of the polymer component of the fibers during the warm-pressing also promotes these effects.

Uniaxial tensile tests of FAS meshes indicated a strong dependence of the tensile strength on the material density (Fig. 4). However, the effect of calcination temperature was not obvious. For all calcination temperatures, the stress-strain curves show a slippage effect in non-compressed low-density material (Fig. 4a), whereas a more brittle behavior in denser meshes is observed (Fig. 4b.c). A noticeable difference was found when the measurements were done along and across the direction of collection of precursor fibrous meshes during the AFES process. Although it was not readily observable in SEM images, this can be related to some level of a macroscopic preferential fiber orientation within the layer [40]. Similar effect has been observed in nanofibrous ceramic meshes derived from AFES precursor fibers [32]. The difference between the behavior of stress-strain curves and magnitudes of strength for those distinct directions for FAS meshes becomes smaller as the density of the material increases. Higher strength, more brittle behavior and smaller effect of the fiber orientation can be explained by a larger number of fusion points between the fibers within the plane and through the thickness of the mesh, as well as by increased inter-fiber friction within the layer. When the nanofibrous network fails due to high stress at the fusion points at 0.7–3.0% strain, the relatively long fibrous segments are released and continue to be pulled out, which leads to a long tail in the stress-strain curves.

The behavior of FAS meshes during the tensile tests is demonstrated in Fig. 5. The samples in photographs were clamped in the direction of the dominant orientation of fibers. Swelling in the through-thickness direction of the FAS sample can be seen around the breakage area even in the densest sample (Fig. 5a,b), which is a consequence of comminution of the fibrous network during deformation, similarly to that observed in ceramic fiber/matrix and woven-fabric/polymer-matrix composites [41,42]. Swelling of the material becomes more pronounced in less dense samples as the material stretches because of little binding between the fibers through the membrane thickness. The buckling, bending, and rotation of longer fibrous segments become easier when the fibers break at high stress points and are pulled out under the load.

The tensile moduli of FAS meshes were calculated from the linear section of the stress-strain curve to establish the scaling relationship between the modulus and density of the material calcined at different temperatures. Similarly, the tensile strength-density scaling relationship was determined from the experimental stress-strain curves using tensile stress at the failure. The results (Fig. 6) reveal a relatively clear trend (Pearson's $R = 91.0$–98.0) within the range of tested mass densities that can be described by a simple power law relationship between the tensile modulus/strength and density in porous and cellular materials [43–45]:

$$E^{*}/E_{\mathrm{dense}} = C \times \left(\rho^{*}/\rho_{\mathrm{dense}}\right)^{n} \tag{3}$$

$$\sigma^{*}/\sigma_{\mathrm{dense}} = C' \times \left(\rho^{*}/\rho_{\mathrm{dense}}\right)^{m} \tag{4}$$

where E^{*}, σ^{*}, ρ^{*} and E_{dense}, σ_{dense}, ρ_{dense} are the moduli, strength, and density for porous and dense states of the material, respectively. The parameters C and C' are the dimensionless constants frequently selected as 1.0, and the exponents n and m vary depending on the cell geometry (*e.g.*, $n = 2$ for open cell, and $n = 3$ for closed cell structures, respectively [43]). For example, Patil et al. found that the modulus of

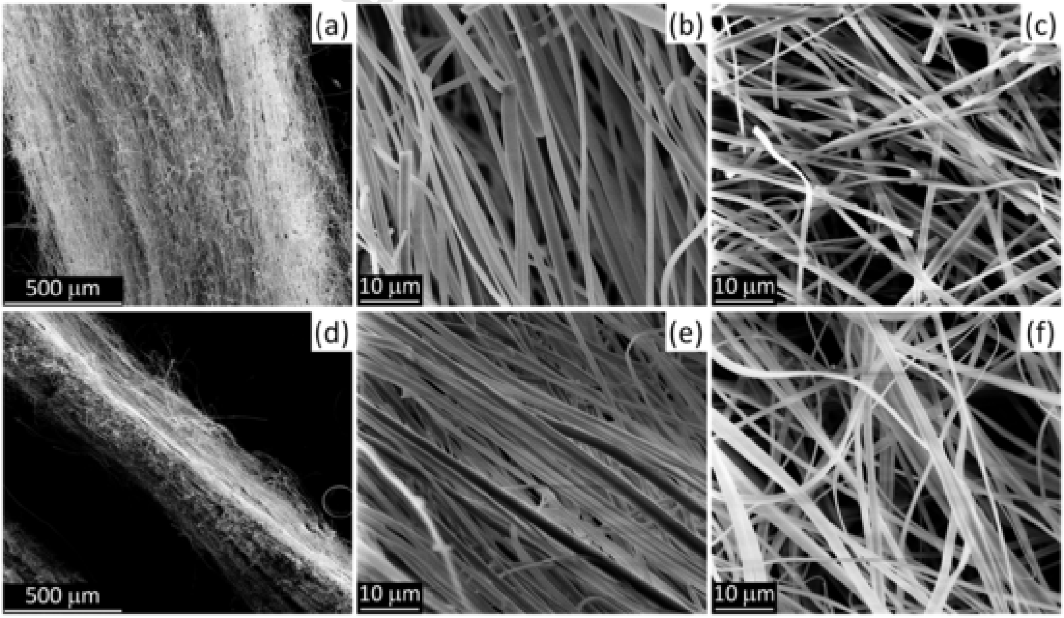

Fig. 3. SEM images of (a) non-compressed and (d) compressed FAS mesh, and the (b,e) corresponding fiber arrangement in the cross-section and (c,f) on the surface of the meshes.

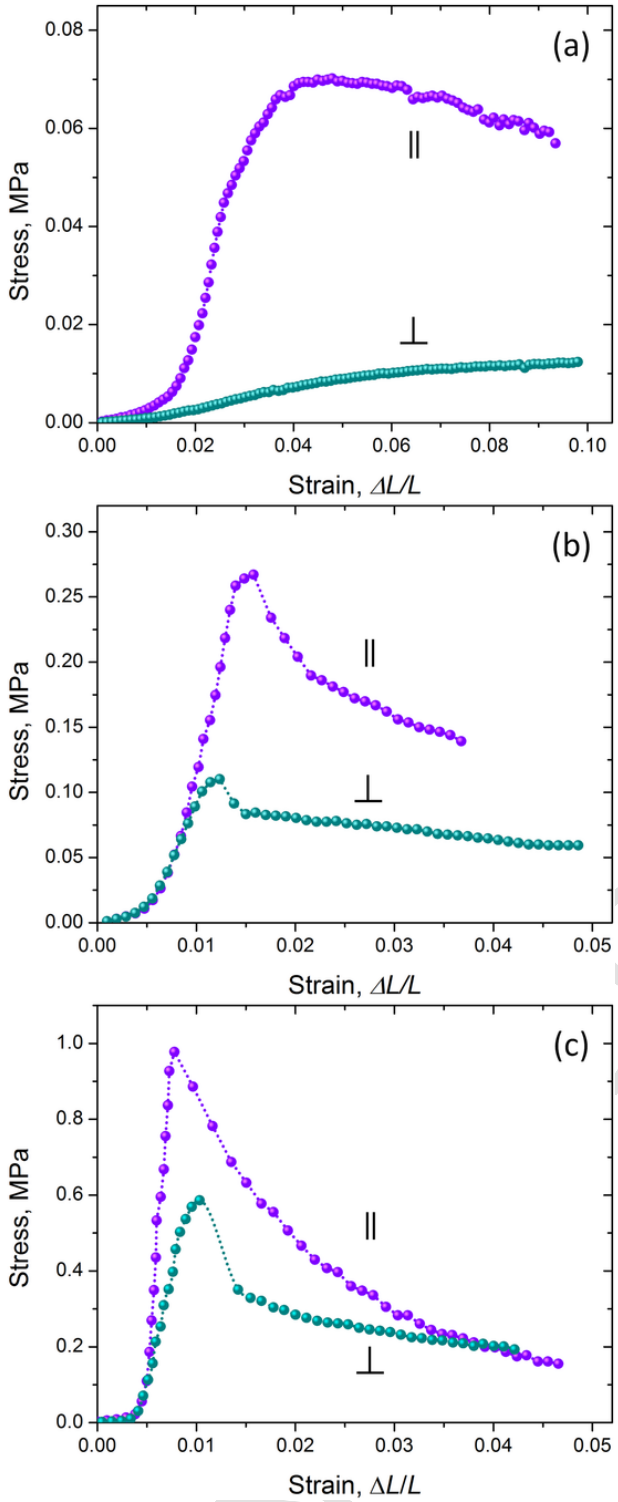

Fig. 4. Tensile stress-strain curves of (a) ~10% compressed ($\varepsilon = 98.7\%$), (b) ~50% compressed ($\varepsilon = 94.8\%$), and (c) ~85% compressed ($\varepsilon = 91.4\%$) 1000 °C calcined FAS meshes along and across the preferred direction of fiber alignment.

amorphous silica aerogels with densities above 0.2 g/cm^3 can be described by the relationship (3) at $n = 3.3 \pm 0.4$ [46], whereas for different sol-gel porous amorphous silica structures the exponent n was in a range of 2.27–2.8 [47]. The present results show that the tensile modulus (Fig. 6a) and strength (Fig. 6b) of AFES derived FAS meshes increased from 2.0 to 580.0 MPa and from 0.05 to 1.4 MPa, respectively, when the density of the material changed from 0.015 to 0.2 g/cm^3 (93.3 to 90.9% total porosity reduction). Using the Young's modulus of 73 GPa, tensile strength of 48 MPa, and the density of 2.196 g/cm^3 for amorphous silica, the modulus and strength data were fitted according to Eqs. (3) and (4) with $n = 2.2$–2.3, $C = 0.77$–1.09 and $m = 1.45$–1.52, $C' = 0.78$–0.83, respectively. According to Ashby [48], the relationships with $n = 2$ and $m = 1.5$ describe the bending-dominated behavior of open-cell foam structures that collapse predominantly by buckling. Although the constants C and C' in Ashby's model were lower (0.2–0.3) than those for FAS meshes, it can be related to the cell shape and cell wall thickness. The latter parameters are determined by the diameter orientation of fibers within the mesh, and the distance between the fusion points within the fibrous structure. From the mechanical perspective, the AFES derived compressed FAS meshes calcined at 600–1000 °C can be realistically described as a mostly open cell porous structure with the properties dominated by bending and buckling. The established tensile property-density relationships in Fig. 6 correlate with the density-dependent swelling behavior of FAS meshes during the tensile tests (Fig. 5). The effect of calcination temperature on the tensile modulus and strength was small, although the denser, 1000 °C calcined samples appear to show slightly higher numbers than those calcined at lower temperatures.

Air transport properties of circular FAS membranes cut from fibrous meshes also strongly depended on the degree of compression of the precursor material. Low-density FAS membranes (porosity above 98.0%) can withstand a maximum pressure gradient ΔP in a range of 18–30 kPa, which correlated with the increase in the calcination temperature from 600 to 1000 °C. Higher density membranes (*e.g.*, porosity $\varepsilon = 92.8$–94.8%) usually ruptured in the range of 8–12 kPa, 20–28 kPa, and 15–18 kPa after the calcination at 600, 800, and 1000 °C, respectively. Regardless of the calcination temperature, the mechanism of the membrane rupture seems to be determined mostly by its microarchitecture at a given density. Fig. 7 shows the photographs of the FAS membranes made from fibrous precursor meshes with different levels of compression after the air permeability tests. The shape of the non-compressed FAS membrane after the rupture (Fig. 7a-c) is consistent with its tensile behavior (Fig. 5e,f) and with the deformation behavior of rather elastic fabric membranes [49]. Compressed membranes with porosity less than 94.8% show brittle fracture (Fig. 7g-i), and the compressed membranes with porosity between 95 and 98.5% exhibit the transition from brittle-to-ductile failure mode (Fig. 7d-f) [50].

Examples of the dependence of air permeability of FAS membranes on the pressure gradient are given in Fig. 8. The maximum Darcy's permeability coefficient K_D in a range of 1.6×10^{-11}–1.2×10^{-12} m^2 was observed at $\Delta P = 1.5$–2.5 kPa. It showed gradual reduction with the increase in ΔP for all membranes with porosities above 93.5%. Such behavior of K_D is associated with the compressibility of the fiber network within the electrospun membrane [27]. Indeed, calcined FAS materials can be compressed by applying pressure in a kPa range, as discussed above. The compressibility reduces when the density of membrane increases, and K_D becomes less dependent on pressure, as observed for 600 °C calcined membrane with $\varepsilon = 93.1\%$ (Fig. 7b). The measured permeability coefficients for FAS membranes are about an order of magnitude higher than those ($K_D = (1.8$–$3) \times 10^{-13}$ m^2) reported for fibrous (160–350 nm fiber diameter) alumina ceramic membranes with similar porosities (92.9–94.5%) calcined from AFES precursor fibers [31]. This can be related to the larger diameters of silica fibers [51] and specifics of the membrane's microarchitecture. The rupture pressures for FAS membranes were also higher when compared to AFES derived nanofibrous alumina membranes [31]. The present results are also consistent with the air permeability data for AFES polyacrylonitrile (PAN)-based polymer fibrous membranes [30] and the results of Kok

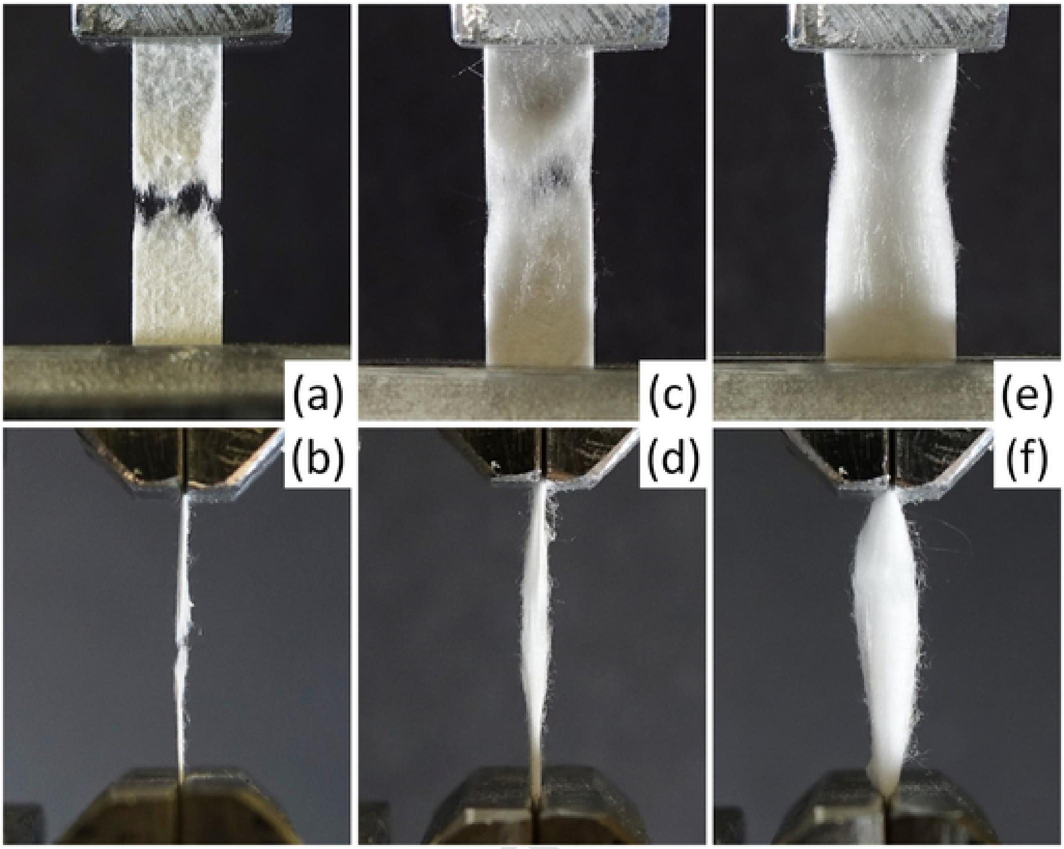

Fig. 5. Photographs of the front and side view of tested samples of (a,b) ~85% compressed, (c,d) ~50% compressed, and (e,f) ~10% compressed fibrous amorphous silica.

and Gostick [52] for DC-electrospun PAN meshes with similar thicknesses, porosities and fiber diameters.

The Darcy's permeability coefficient K_D is related to both the pore and particle (fiber) diameters, and it is normally between 10^{-13} to 10^{-9} m^2 for many gel-cast and fibrous membrane materials with 50–75% porosity [27,36,53–55]. The relationship between the Darcy's permeability coefficient, porosity, and particle size is set, under numerous assumptions, by Ergun's relationship [56,57] as

$$K_D = \varepsilon^3 d_{\text{particle}}{}^2 / \left[150(1-\varepsilon)^2\right] \tag{5}$$

where d_{particle} is the effective diameter of a particle in the porous media, and the particle diameter is related to the pore diameter as.

$$d_{\text{particle}} = 1.5\,(1-\varepsilon)\,d_{\text{pore}}/\varepsilon \tag{6}$$

Combining these two equations and using the experimental maximum K_D numbers for all tested FAS samples of known porosity (Fig. 8), the effective pore and fiber diameters have been estimated and plotted in Fig. 9. Although the physical average fiber diameter in calcined FAS is approximately 500 nm, as measured from SEM images, the effective diameter doubles when the porosity of compressed membranes is reduced from ~99 to 93%. This can be associated with the observed fiber bundling and partial fusion in warm-pressed precursor fibers, which can also be seen in SEM images of the resulting FAS meshes (Fig. 3). Although the apparent increase in diameter should lead to higher permeability numbers, the simultaneous pore size reduction prevails when the total porosity decreases. The effect of the warm-pressing procedure on the resulting FAS mesh microarchitecture can explain the relatively higher K_D coefficients when compared to other electrospun materials with similar fiber diameters and porosities [27,30,31,52]. It appears that the increase of the effective fiber diameter (particle size) diminishes at a higher degree of fibrous mesh compression. It can be predicted further that the reduction of K_D of FAS membranes at higher ΔP across the membrane is related mainly to the pore closure when the parallel stacks of two-dimensional fibrous layers come closer.

To validate the trends observed in Fig. 8 and Fig. 9, the effect of porosity on the dimensionless permeability parameter K_D/d^2 was analyzed using several empirical fitting models for transverse flow through fibrous structures [58,59]. The K_D/d^2 numbers were obtained using the calculated effective fiber diameter for FAS meshes, and the results are displayed in Fig. 10 together with the fitting curves. The best fitting curve was obtained by using Kozeny-Carman equation in the form proposed for random fiber structures [58] as follows:

$$K_D/d^2 = \varepsilon^3 / \left[16K_c(1-\varepsilon)^2\right] \tag{7}$$

where d is the particle diameter and K_c is the Kozeny constant. The fitting curve was obtained using Eq. (7) at $K_c = 9.5$. This number compares reasonably well with the predictions for the Kozeny constant for 2-D (7.1–8.9) and 1-D (8.4–12.5) fibrous structures, with porosities between 80 and 100%, when the flow is directed perpendicular to the plane or fiber in a fibrous layer. Although the obtained magnitude of Kozeny constant is a little larger than those based on Johnson's transport parameter-based predictions for a random 2-D fibrous network [58], it is reasonable because some degree of 1-D fiber alignment is present in the tested FAS structures (Fig. 4). Alternatively, both the Johnson [58] and Tamayol-Bahrami [59] models can provide the same match for the experimental data when the empirical constants 0.0065 (instead of 0.01064) and 0.0107 (instead of 0.008) are used, respectively. Neither model was able to provide a good fit if the change in the effective fiber diameter associated with compression of FAS structures was not considered.

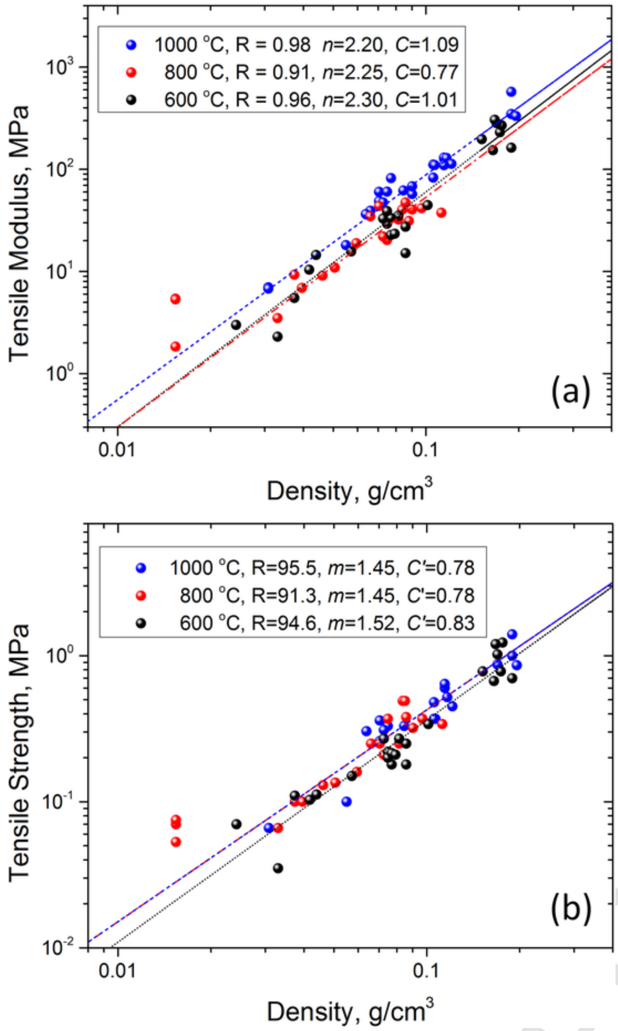

Fig. 6. Tensile modulus (a) and strength (b) *vs* mass density data, and fitting parameters for the scaling law of FAS meshes at different magnitudes of compression and calcination temperatures.

4. Conclusions

The results of this study demonstrate that the highly porous fibrous amorphous silica meshes and membranes with controlled mechanical strength and air permeability can be efficiently prepared from the precursor fibers produced by a high-yield free-surface AFES process. Both the high density of the propagating fibrous flows and fiber bundling can influence the structure of the collected fibrous assemblies and their subsequent processing into the fibrous amorphous silica. It has been shown that the mechanical and transport properties of FAS membranes can be tailored by using a combination of mild thermal and pressure treatment of the precursor fibrous meshes before the calcination step. The degree of the precursor material's compression determines the resulting porosity, effective fiber diameter, and microarchitecture of the calcined FAS meshes and membranes. The 0.1–1.5 mm thick FAS membranes are flexible and tend to compress further under the flow of gas, which results in lower air permeability numbers when the pressure drop across the membrane increases. The latter effect is reduced when the membranes were below 93% porosity. When the porosity-dependent change in effective fiber diameter is considered, the permeability of fabricated membranes follows the models developed for two-dimensional fibrous architectures with some degree of fiber alignment within the stacked layers. The calcination temperature of the FAS membrane seems to have both a moderate effect on the mechanical performance and little effect on air flow permeability.

The attained porosity, tensile modulus, strength, and flow permeability numbers of the prepared FAS membranes make them suitable for many microfiltration applications. Furthermore, a combination of the high-yield AFES process with an appropriate intermediate thermal and pressure treatment procedure of as-spun materials can be a promising approach for the fabrication of many porous nano- and micro-fibrous glass, ceramic, and other structures.

Declaration of Competing Interest

The authors declare that they have no known competing financial interests or personal relationships that could have appeared to influence the work reported in this paper.

Acknowledgements

This work has been supported by the National Science Foundation (NSF) [Grant number DMR-1708600]. Justin Tchernov thanks the support from the NSF International Research Experience for Students (IRES) Program [Grant number OISE-1558268] and from the EU Erasmus + Program. The authors thank Dr. Waldemar Maniukiewicz for XRD data.

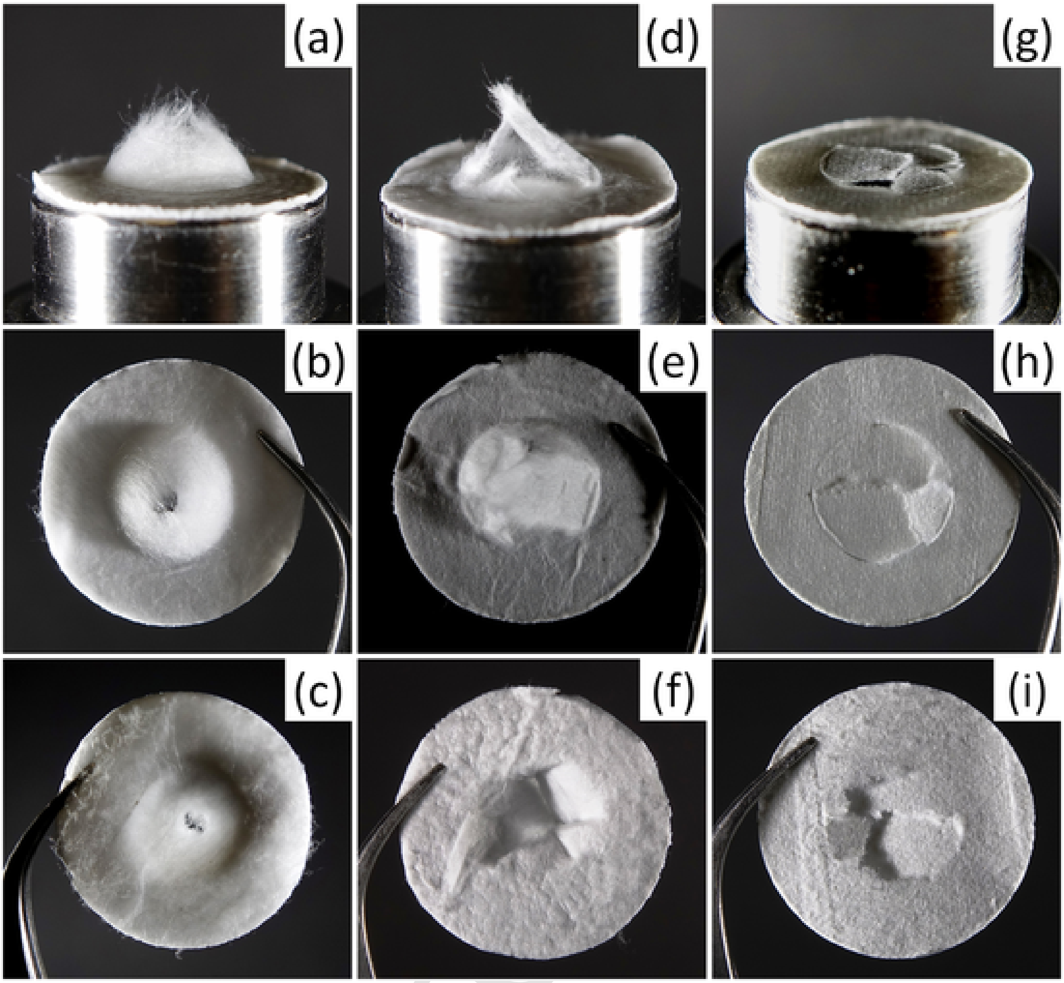

Fig. 7. Photographs of the fibrous amorphous silica (FAS) membrane failure (side, front, and back view) during the air permeability tests of (a-c) ~10%, (d-f) ~50%, and (g-i) ~85% compressed FAS membranes.

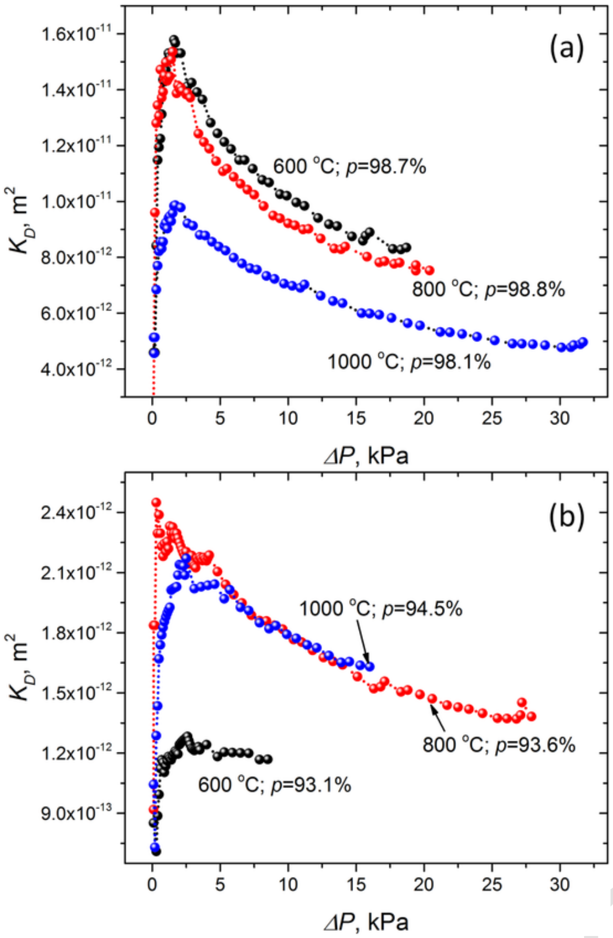

Fig. 8. Darcy's air permeability coefficients of FAS membranes with (a) less than 30% and (b) more than 70% compression from the initial thickness after calcination at different temperatures.

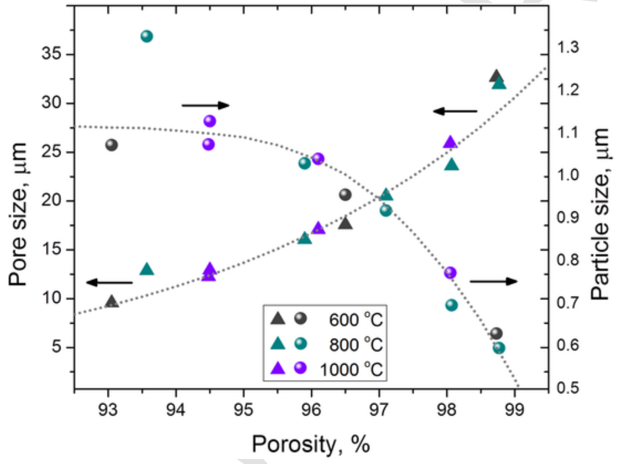

Fig. 9. Effective pore and particle (fiber) size *vs* porosity of FAS meshes.

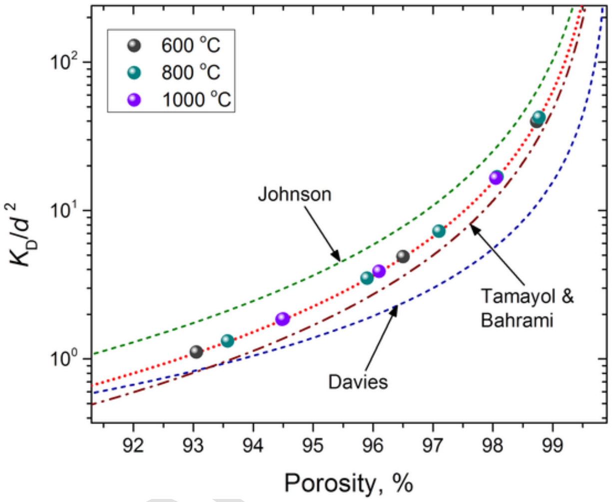

Fig. 10. Dimensionless permeability *vs* porosity of FAS membranes. Fitted curves include Davies ($K_D/d^2 = [64\varepsilon^{3/2}(1 + 56\varepsilon^2)]^{-1}$), Johnson ($K_D/d^2 = 0.01064[\varepsilon\ (1+\ \varepsilon)/(1-\varepsilon)]^{-1}$), Tamayol-Bahrami ($K_D/d^2 = 0.008\varepsilon^{0.5}[(0.25\pi/(1-\varepsilon))^2–0.5\pi/(1-\varepsilon)+1]$), and Kozeny-Carman at $K_c = 9.5$.

References

[1] M. Zhu, J. Han, F. Wang, W. Shao, R. Xiong, Q. Zhang, H. Pan, Y. Yang, S.K. Samal, F. Zhang, C. Huang, Electrospun nanofibers membranes for effective air filtration, Macromol. Mater. Eng. 302 (2017), doi:10.1002/mame.201600353 1600353.

[2] S. Zhang, H. Liu, F. Zuo, X. Yin, J. Yu, B. Ding, A controlled design of ripple-like polyamide-6 nanofiber/nets membrane for high-efficiency air filter, Small. 13 (2017), doi:10.1002/smll.201603151 1603151.

[3] H. Matsumoto, A. Tanioka, Functionality in electrospun Nanofibrous membranes based on Fiber's size, surface area, and molecular orientation, Membranes 1 (2011) 249–264, doi:10.3390/membranes1030249.

[4] X. Wang, B.S. Hsiao, Electrospun nanofiber membranes, Curr. Opin. Chem. Eng. 12 (2016) 62–81, doi:10.1016/j.coche.2016.03.001.

[5] L. Wang, Z. Wang, Y. Sun, X. Liang, H. Xiang, Sb2O3 modified PVDF-CTFE electrospun fibrous membrane as a safe lithium ion battery separator, J. Membr. Sci. 572 (2019) 512–519, doi:10.1016/j.memsci.2018.11.041.

[6] F.E. Ahmed, B.S. Lalia, R. Hashaikeh, A review on electrospinning for membrane fabrication: challenges and applications, Desalination 356 (2015) 15–30, doi:10.1016/j.desal.2014.09.033.

[7] Y. Liao, C.H. Loh, M. Tian, R. Wang, A.G. Fane, Progress in electrospun polymeric nanofibrous membranes for water treatment: fabrication, modification and applications, Prog. Polym. Sci. 77 (2018) 69–94, doi:10.1016/j.progpolymsci.2017.10.003.

[8] L. Persano, A. Camposeo, C. Tekmen, D. Pisignano, Industrial upscaling of electrospinning and applications of polymer nanofibers: a review, Macromol. Mater. Eng. 298 (2013) 504–520, doi:10.1002/mame.201200290.

[9] D. Malwal, P. Gopinath, Fabrication and applications of ceramic nanofibers in water remediation: a review, Critical Rev. Env. Sci. Technol. 46 (2016) 500–534, doi:10.1080/10643389.2015.1109913.

[10] X. Wang, L. Dou, Z. Li, L. Yang, J. Yu, B. Ding, Flexible hierarchical ZrO2 nanoparticle-embedded SiO2 nanofibrous membrane as a versatile tool for efficient removal of phosphate, ACS Appl. Mater. Interfaces 8 (2016) 34668–34676, doi:10.1021/acsami.6b11294.

[11] X. Mao, Y. Bai, J. Yu, B. Ding, J. Ferreira, Flexible and highly temperature resistant polynanocrystalline zirconia nanofibrous membranes designed for air filtration, J. Am. Ceram. Soc. 99 (2016) 2760–2768, doi:10.1111/jace.14278.

[12] J. Song, X. Wang, J. Yan, J. Yu, G. Sun, B. Ding, Soft Zr-doped TiO2 nanofibrous membranes with enhanced photocatalytic activity for water purification, Sci. Rep. 7 (2017) 1636, doi:10.1038/s41598-017-01969-w.

[13] Y. Tang, Z. Liu, K. Zhao, S. Fu, Adsorption and separation properties of positively charged ZrO2 nanofibrous membranes fabricated by electrospinning, RSC Adv. 7 (2017) 42505–42512, doi:10.1039/c7ra08227d.

[14] M.C. Santos, Y.A. Elabd, Y. Jing, B.P. Chaplin, L. Fang, Highly porous Ti4O7 reactive electrochemical water filtration membranes fabricated via electrospinning/electrospraying, AICHE J. 62 (2016) 508–524, doi:10.1002/aic.15093.

[15] W. Fu, Y. Dai, J. Tian, C. Huang, Z. Liu, K. Liu, L. Yin, F. Huang, Y. Lu, Y. Sun, In situ growth of hierarchical Al2O3 nanostructures onto TiO2 nanofibers surface: super-hydrophilicity, efficient oil/water separation and dye-removal, Nanotechnol. 29 (2018), doi:10.1088/1361-6528/aac9ab 345607.

[16] M.H. Tai, P. Gao, B.Y.L. Tan, D.D. Sun, J.O. Leckie, Highly efficient and flexible electrospun carbon-silica nanofibrous membrane for ultrafast gravity-driven oil-water separation, ACS Appl. Mater. Interfaces 6 (2014) 9393–9401, doi:10.1021/am501758c.

[17] N. Wu, B. Wang, Y. Wang, Enhanced mechanical properties of amorphous SiOC nanofibrous membrane through in situ embedding nanoparticles, J. Am. Ceram. Soc. 101 (2018) 4763–4772, doi:10.1111/jace.15732.

[18] X. Wang, L. Dou, L. Yang, J. Yu, B. Ding, Hierarchical structured MnO2@SiO2 nanofibrous membranes with superb flexibility and enhanced catalytic performance, J. Hazard. Mater. 324 (2017) 203–212, doi:10.1016/j.jhazmat.2016.10.050.

[19] Y. Si, C. Yan, F. Hong, J. Yu, B. Ding, A general strategy for fabricating flexible magnetic silica nanofibrous membranes with multifunctionality, Chem. Commun. 51 (2015) 12521–12524, doi:10.1039/c5cc03718b.

[20] Y. Tang, Z. Liu, K. Zhao, S. Fu, Positively charged and flexible SiO2@ZrO2 nanofibrous membranes and their application in adsorption and separation, RSC Adv. 8 (2018) 13018–13025, doi:10.1039/c8ra01899e.

[21] L. Yang, A. Raza, Y. Si, X. Mao, Y. Shang, B. Ding, J. Yu, S.S. Al-Deyab, Synthesis of superhydrophobic silica nanofibrous membranes with robust thermal stability and flexibility via in situ polymerization, Nanoscale. 4 (2012) 6581–6587, doi:10.1039/c2nr32095a.

[22] Y. Si, X. Mao, H. Zheng, J. Yu, B. Ding, Silica nanofibrous membranes with ultra-softness and enhanced tensile strength for thermal insulation, RSC Adv. 5 (2015) 6027–6032, doi:10.1039/c4ra12271b.

[23] X. Mao, Y. Si, Y. Chen, L. Yang, F. Zhao, B. Ding, J. Yu, Silica nanofibrous membranes with robust flexibility and thermal stability for high-efficiency fine particulate filtration, RSC Adv. 2 (2012) 12216–12223, doi:10.1039/c2ra22086e.

[24] Z. Zhu, Z. Li, L. Zhong, R. Zhang, F. Cui, W. Wang, Dual-biomimetic superwetting silica nanofibrous membrane for oily water purification, J. Membr. Sci. 572 (2019) 73–81, doi:10.1016/j.memsci.2018.10.071.

[25] S. Yang, Y. Si, Q. Fu, F. Hong, J. Yu, S.S. Al-Deyab, M. El-Newehy, B. Ding, Superwetting hierarchical porous silica nanofibrous membranes for oil/water microemulsion separation, Nanoscale. 6 (2014) 12445–12449, doi:10.1039/c4nr04668d.

[26] E. Loccufier, J. Geltmeyer, L. Daelemans, D.R. D'hooge, K. De Buysser, K. De Clerck, Silica nanofibrous membranes for the separation of heterogeneous azeotropes, Adv. Funct. Mater. 28 (2018), doi:10.1002/adfm.201804138 1804138.

[27] L.T. Choong, Z. Khan, G.C. Rutledge, Permeability of electrospun fiber mats under hydraulic flow, J. Membr. Sci. 451 (2014) 111–116, doi:10.1016/j.memsci.2013.09.051.

[28] P. Pokorny, E. Košťáková, F. Sanetmik, P. Mikes, J. Chvojka, T. Kalous, M. Bilek, K. Pejchar, J. Valtera, D. Lukaš, Effective AC needleless and collectorless electrospinning for yarn production, Phys. Chem. Chem. Phys. 16 (2014) 26816–26822, doi:10.1039/c4cp04346d.

[29] C. Lawson, A. Stanishevsky, M. Sivan, P. Pokorny, D. Lukáš, Rapid fabrication of poly(ε-caprolactone) fibers using needleless alternating current electrospinning, J. Appl. Polym. Sci. 133 (2016), doi:10.1002/app.43232 43232.

[30] K. Paulett, W.A. Brayer, K. Hatch, T. Kalous, J. Sewell, T. Liavitskaya, S. Vyazovkin, F. Liu, D. Lukáš, A. Stanishevsky, Effect of nanocrystalline cellulose addition on needleless alternating current electrospinning and properties of nanofibrous polyacrylonitrile meshes, J. Appl. Polym. Sci. 135 (2018), doi:10.1002/app.45772 45772.

[31] A. Stanishevsky, W.A. Brayer, P. Pokorny, T. Kalous, D. Lukáš, Nanofibrous alumina structures fabricated using high-yield alternating current electrospinning, Ceram. Int. 42 (2016) 17154–17161, doi:10.1016/j.ceramint.2016.08.003.

[32] A. Stanishevsky, R. Yager, J. Tomaszewska, M. Binczarski, W. Maniukiewicz, I. Witońska, D. Lukaš, Structure and mechanical properties of nanofibrous ZrO2 derived from alternating field electrospun precursors, Ceram. Int. 45 (2019) 18672–18682, doi:10.1016/j.ceramint.2019.06.092.

[33] J. Geltmeyer, J. De Roo, F. Van den Broeck, J.C. Martins, K. De Buysser, K. De Clerck, The influence of tetraethoxysilane sol preparation on the electrospinning of silica nanofibers, J. Sol-Gel Sci. Technol. 77 (2016) 453–462, doi:10.1007/s10971-015-3875-1.

[34] B.D. Cullity, Elements of XRD, Second ed., Addison-Wesley, Reading, MA, USA, 1978.

[35] F. Dullien, Porous Media – Fluid Transport and Pore Structure, Academic Press, New York, 1979.

[36] J.A. Fernando, D.D.L. Chung, Pore structure and permeability of an alumina fiber filter membrane for hot gas filtration, J. Porous. Mater. 9 (2002) 211–219, doi:10.1023/A:1020991002430.

[37] T. Isobe, Y. Kameshima, A. Nakajima, K. Okada, Y. Hotta, Gas permeability and mechanical properties of porous alumina ceramics with unidirectionally aligned pores, J. Eur. Ceram. Soc. 27 (2007) 53–59, doi:10.1016/j.jeurceramsoc.2006.02.030.

[38] A.M. Drews, L. Cademartiri, G.M. Whitesides, K.J.M. Bishop, Electric winds driven by time oscillating corona discharges, J. Appl. Phys. 114 (2012), doi:10.1063/1.4824748 143302.

[39] J.R. Martínez, S. Palomares-Sánchez, G. Ortega-Zarzosa, F. Ruiz, Y. Chumakov, Rietveld refinement of amorphous SiO2 prepared via sol–gel method, Mater. Lett. 60 (2006) 3526–3529, doi:10.1016/j.matlet.2006.03.044.

[40] R.L. Mauck, M. Brendon, B.S. Baker, L. Nandan, M.S. Nerurkar, J.A. Burdick, W.J. Li, R.S. Tuan, D.M. Elliott, Engineering on the straight and narrow: the mechanics of nanofibrous assemblies for fiber-reinforced tissue regeneration, Tissue Eng. Part B. 15 (2009) 171–193 (doi:10.1089 = ten.teb.2008.0652).

[41] C.G. Levi, J.Y. Yang, B.J. Dalgleish, F.W. Zok, A.G. Evans, Processing and performance of an all-oxide ceramic composite, J. Am. Ceram. Soc. 81 (1998) 2077–2086, doi:10.1111/j.1151-2916.1998.tb02590.x.

[42] G. Odegard, K. Searles, M. Kumosa, A continuum elastic–plastic model for woven-fabric/polymer-matrix composite materials under biaxial stresses, Compos. Sci. Technol. 61 (2001) 2501–2510, doi:10.1016/S0266-3538(01)00168-3.

[43] L.J. Gibson, M.F. Ashby, Cellular Solids: Structure and Properties, Second ed., Cambridge University Press, Cambridge, UK, 1997.

[44] H. Fan, C. Hartshorn, T. Buchheit, D. Tallant, R. Assink, R. Simpson, D.J. Kissel, D.J. Lacks, S. Torquato, C.J. Brinker, Modulus-density scaling behaviour and framework architecture of nanoporous self-assembled silicas, Nat. Mater. 6 (2007) 418–423, doi:10.1038/nmat1913.

[45] P. Colombo, J.R. Hellmann, D.L. Shelleman, Mechanical properties of silicon oxycarbide ceramic foams, J. Am. Ceram. Soc. 84 (2001) 2245–2251, doi:10.1111/j.1151-2916.2001.tb00996.x.

[46] S.P. Patil, A. Rege, M. Sagardas, B.M. Itskov, Mechanics of nanostructured porous silica aerogel resulting from molecular dynamics simulations, J. Phys. Chem. B 121 (2017) 5660–5668, doi:10.1021/acs.jpcb.7b03184.

[47] J.M. Rimsza, J. Du, Structural and mechanical properties of nanoporous silica, J. Am. Ceram. Soc. 97 (2014) 772–781, doi:10.1111/jace.12707.

[48] M.F. Ashby, Cellular solids – scaling of properties, in: M. Scheffler, P. Colombo (Eds.), Cellular Ceramics: Structure, Manufacturing, Properties and Applications, WILEY-VCH Weinheim, 2005, pp. 3–17.

[49] P.W. Gibson, K. Desabrais, T. Godfrey, Dynamic permeability of porous elastic fabrics, J. Eng. Fibers and Fabrics. (2012) 29–36 7 Sp. Iss..

[50] C.T. Koh, M.L. Oyen, Toughening in electrospun fibrous scaffolds, APL Mater. 3 (2015) 14908, doi:10.1063/1.4901450.

[51] R. Vallabh, P. Banks-Lee, A.F. Seyam, New approach for determining tortuosity in fibrous porous media, J. Eng. Fibers and Fabrics. 5 (2010) 7–15.

[52] M.D.R. Kok, J.T.J. Gostick, Transport properties of electrospun fibrous membranes with controlled anisotropy, J. Membr. Sci. 473 (2015) 237–244, doi:10.1016/j.memsci.2014.09.017.

[53] J. Seuba, S. Deville, C. Guizard, A.J. Stevenson, Gas permeability of ice-templated, unidirectional porous ceramics, Sci. Technol. Adv. Mater. 17 (2016) 313–323, doi:10.1080/14686996.2016.1197757.

[54] L. Simão, R.F. Caldato, M.D.M. Innocentini, O.R.K. Montedo, Permeability of porous ceramic based on calcium carbonate as pore generating agent, Ceram. Int. 41 (2015) 4782–4788, doi:10.1016/j.ceramint.2014.12.031.

[55] J. Kim, J.H. Ha, J. Lee, I.H. Song, Effect of pore structure on gas permeability constants of porous alumina, Ceram. Int. 45 (2019) 5231–5239, doi:10.1016/j.ceramint.2018.11.219.

[56] Y. Bruni, L. Garrido, E. Aglietti, Application of the Ergun's equation in porous ceramic based on CaO-stabilized ZrO2, Procedia Mater. Sci. 1 (2012) 418–424, doi:10.1016/j.mspro.2012.06.056.

[57] M.D.M. Innocentini, V.R. Salvini, A. Macedo, V.C. Pandolfelli, Prediction of ceramic foams permeability using Ergun's equation, Mater. Res. 2 (1999) 283–289, doi:10.1590/S1516-14391999000400008.

[58] M.M. Tomadakis, T.J. Robertson, Viscous permeability of random fiber structures: comparison of electrical and diffusional estimates with experimental and analytical results, J. Compos. Mater. 39 (2005) 163–188, doi:10.1177/0021998305046438.

[59] A. Tamayol, M. Bahrami, Transverse permeability of fibrous porous media, Phys. Rev. E Stat. Nonlinear Soft Matter Phys. 83 (2011), doi:10.1103/PhysRevE.83.046314 046314.